Pergamon

Journal of Structural Geology, Vol. 19, Nos 3–4, pp. 551 to 566, 1997

0191-8141/97 $17.00 + 0.00

PII: S0191-8141(96)00109-5

Numerical modeling of fold initiation at thrust ramps

LUTHER M. STRAYER and PETER J. HUDLESTON

Department of Geology and Geophysics, University of Minnesota, Minneapolis, MN 55455, U.S.A.

(*Received* 2 *February* 1996; *accepted in revised form* 10 *November* 1996)

Abstract—The movement of the hangingwall over the footwall at thrust ramps produces a variety of structures found commonly at different scales in fold-and-thrust belts. The nature of the structure depends on the relative rigidity of the hangingwall and footwall, friction along the fault, fault 'dip', fault displacement, and the boundary conditions of the deformation. Structures include fault-bend style folds, fault-propagation style folds and wedge folds. We investigate the initial stages of development of such structures using the finite-difference code FLAC. The rock layers are represented as continua with elastic–plastic Mohr–Coulomb constitutive relations, and the fault and bounding bedding planes are assigned normal and shear stiffnesses and coefficients of friction. Under conditions with all layers compressed, antisymmetric fault-propagation style folds develop in both the hangingwall and footwall. With rigid footwall and restricted far-field slip in the hangingwall, a single fault-propagation style fold develops. With far-field displacement of the hangingwall allowed, broader antisymmetric wedge folds develop if hangingwall and footwall are deformable, and a single fault-bend style fold develops if the footwall is rigid. All structures become accentuated with increasing slip on the fault. Where both hangingwall and footwall are deformable, the deformation reduces the ramp angle and tends to minimize distortion of the rock adjacent to the fault. Fault-propagation style folds, paired wedge folds and fault-bend style folds are common in nature, and small-scale examples can be found in various stages of development. Continued slip on thrust faults may lead to the mature structures commonly seen in fold-and-thrust belts.

INTRODUCTION

Folding and faulting are intimately related in fold-and-thrust belts, and they represent the effects of combined brittle and ductile processes of deformation. Several distinct structural associations have been described. These include fault-bend folds (Suppe, 1983, 1985, fig. 9-43), in which the fold forms as a consequence of the hangingwall conforming to the shape of the footwall where the fault passes from one flat to another at a ramp. A second type is a fault-propagation fold (Suppe and Medwedeff, 1984; Suppe, 1985, fig. 9-47) in which the fold forms to accommodate the loss of displacement at a fault tip at a thrust ramp. A detachment fold (Jamison, 1987) is formed at a fault tip in a similar way, but there is no association with a ramp. In all the above, the folds form as a consequence of the thrusting. In other cases the folds form first and the thrusts later (Dixon and Liu, 1992). In break-thrust folds (Fischer *et al.*, 1992; Woodward, 1992), which are of this type, a thrust is generally parallel to bedding in hangingwall and footwall, but cuts across bedding at a high angle through the limb of a fold.

Where folds form as a consequence of thrusting, it is usually the hangingwall that is assumed to take up all or most of the deformation (e.g. the structures illustrated by McClay, 1992, pp. 419–433). This does not have to be the case, as has been emphasized by Ramsay (1992). Also, a complex association of folds and faults may develop in duplexes as a result of the progressive collapse of either the hangingwall or footwall (Dahlstrom, 1970; Boyer and Elliott, 1982). Where thrusts and folds develop in sequence, there is the problem of establishing the order of stacking (i.e. following a piggyback sequence or reverse or more complex order), and of establishing whether individual folds are associated with the footwall or the hangingwall. There is substantial literature on interpreting structures in fold-and-thrust belts (Dahlstrom, 1969; Boyer and Elliott, 1982; Boyer, 1986; Jamison, 1987; McClay, 1992).

The relationship between a thrust fault and associated folds is most clearly seen when the displacement is small, such that the initial configuration can be established with some confidence. In addition, the geometrical relationships are most clear in small-scale structures exposed in outcrop. Figure 1(a) illustrates an early stage of ramp-related folding where a thrust cuts up from the base to the top of a competent sandstone layer. In this case both hangingwall and footwall have undergone similar amounts of deformation (see also Ramsay, 1992, fig. 15b). A more advanced stage is shown in Fig. 1(b), with a well-developed ramp anticline in the hangingwall. The structures shown in Fig. 1(a & b) were referred to by Cloos (1961) as wedges and the process that produced them as wedging.

Most of the work on folding in fold-and-thrust belts has been directed towards establishing geometrical relationships of folds and thrusts and the construction of permissible cross-sections based on limited data and principles of section balancing (Dahlstrom, 1969; Elliott and Johnson, 1980; Mitra and Namson, 1989). The rules of such reconstruction usually involve no change in bed length or thickness, straight limbs, and a consequent accommodation of folding by slip between layers and kink-fold geometry. Deformation in such circumstances is according to the well-defined rules of flexural slip folding (Ramsay, 1967, p. 392). Although significant

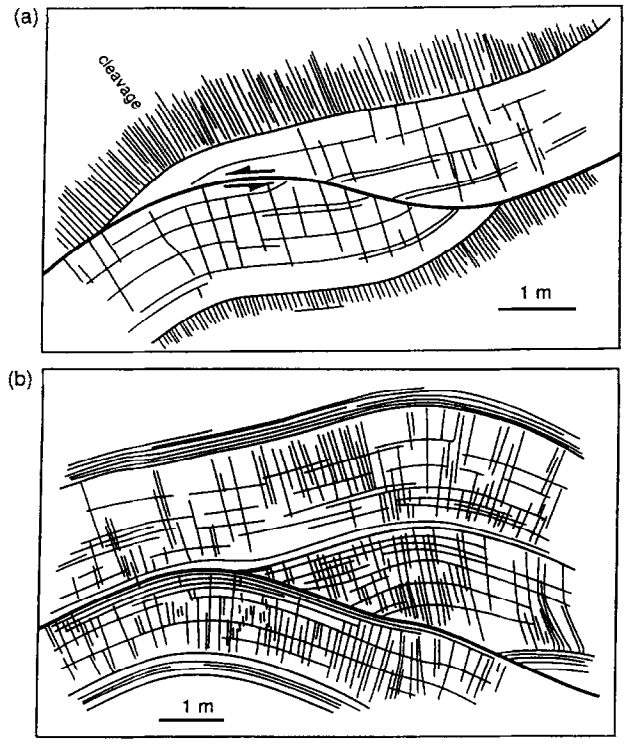

Fig. 1. Field examples of fault-related folds (after Cloos, 1961, 1964) from the Silurian Bloomsburg Formation, western Maryland. (a) Wedge fold in a sandstone bed in cleaved shales; (b) ramp anticline near the hinge of an anticline.

advances have been made in the understanding of the mechanics of thrust systems as a whole (Elliott, 1976; Chapple, 1978; Davis *et al.*, 1983; Dahlen *et al.*, 1984; Dahlen and Barr, 1989), there has been relatively little work on the mechanics of associated faulting and folding, certainly in part because it is not easy to generate analytical models that allow for both brittle and ductile behavior.

Initial work in studying the mechanics of folding in hangingwalls was done by using an analytical approach to analyze the flow of a viscous hangingwall over a rigid (Berger and Johnson, 1980) or deformable (Kilsdonk and Fletcher, 1989) footwall. This work showed the importance of fault drag on the shape of the ramp-related fold. In recent years, finite-element models based on viscous flow laws have been used to show the importance of anisotropy on the shape of and strain distribution in ramp-related folds (Lan and Hudleston, 1995). Also, finite-element models of fault-bend folding have been developed (Reddy *et al.*, 1982; Apperson and Goff, 1991; Erickson, 1995) in which rock layers and faults can be assigned more realistic material properties, allowing for deformation of the rock by viscous or plastic flow, and with faults assigned normal and shear elastic stiffnesses and coefficient of friction. Erickson and Jamison (1995) and Erickson (1995) combined viscous and plastic behavior in their models, arguing that the viscous behavior simulated pressure solution and the plastic behavior cataclasis, both important processes in fold-and-thrust belts. They showed how deformation mechanisms from these different behaviors could be expected to vary around fault-bend folds.

Another fruitful approach to studying fault-related folding has been by the application of physical models using analog materials and rocks. Chester *et al.* (1988, 1991) performed unscaled experiments to study ramp-related folding in a sandstone layer, in which deformation occurred by microfracturing and faulting. They showed that fold development was strongly dependent on the strength ratio given by 'resistance to foreland translation' relative to 'resistance to internal deformation'. When this ratio is low, fault-bend folding results; when it is high, fault-propagation folding is favored. Dixon and Liu (1992) and Liu and Dixon (1995) have performed scaled analog modeling using Plasticine and silicone putty. Buckling played a key role in their models in localizing stresses that initiated faulting and duplex formation.

In this paper we make use of the finite-difference program FLAC (Fast Lagrangian Analysis of Continua) (Cundall and Board, 1988) to study the initiation of folding and plastic deformation associated with a ramp in a pre-existing thrust fault. A most interesting feature of this code is its ability to simulate localization of deformation. This arises from the specification in the constitutive relationships of non-associated plasticity (Vermeer and de Borst, 1984). This can be considered to simulate the initiation of faulting in the upper crust. Cundall (1990), for example, has shown how FLAC can simulate the development of conjugate faults during rifting and graben formation. Features of FLAC and its application in our modeling are described in the next section.

Our models were inspired by outcrop-scale folds in the early stages of development associated with ramps in stiff layers throughout Mesozoic strata in southwestern Montana (Fig. 2) as well as by published examples from Cloos (1961, 1964) (also Fig. 1), Eisenstadt and De Paor (1987), Martinez-Torres *et al.* (1994) and others. Although the models are to some extent scale-independent (if we neglect the effect of gravity), we have chosen to model outcrop-scale structures in these simulations because such structures provide the best control on geometry and distribution of fabric and smaller-scale fractures.

NUMERICAL MODELING

FLAC is a two-dimensional explicit finite-difference code designed for geomechanics applications (Cundall and Board, 1988; Coetzee *et al.*, 1995). It has many similarities to and several advantages over finite-element methods (Reddy, 1993) that make it ideal for geologic modeling. The explicit finite-difference formulation results in there being no 'stiffness' matrices to be inverted during each time-step. This is a great computational advantage that to some degree is offset by the need for

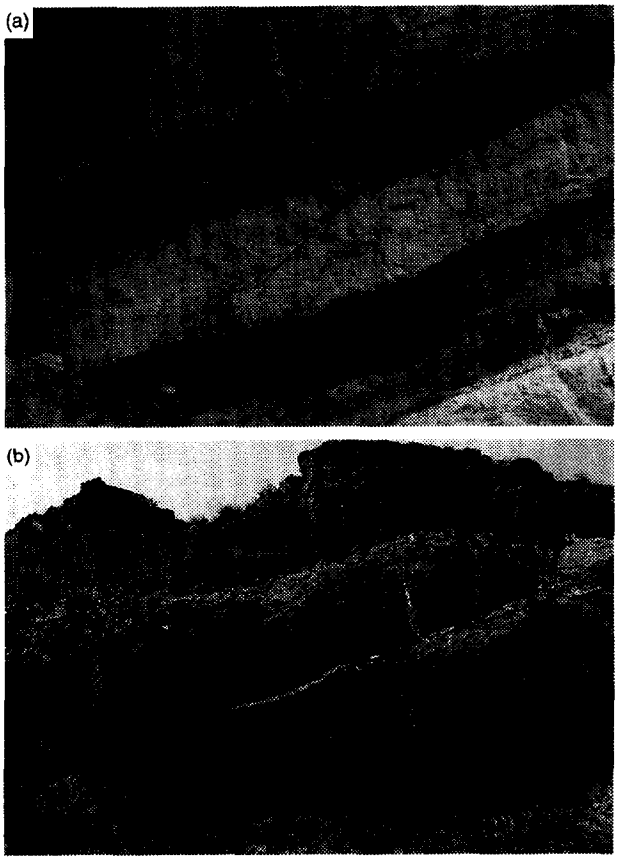

Fig. 2. Early-stage wedge folds in limestone beds within marls from the Cretaceous Kootenai Formation, south-western Montana. (a) At the earliest stage of fault slip. The incipient thrust ramp is nearly planar, and there is only the first hint of brittle–plastic deformation at the tips of the wedges. Knife for scale is 10 cm. (b) A more evolved wedge fold showing reduced ramp angle, and the development of a ramp anticline in the hangingwall. Rock hammer for scale.

small time-steps. In finite-element models all nodes are in communication during each time-step, and iteration is necessary to achieve compatibility and equilibrium. In the FLAC method, the time-step must be small enough to ensure that the physical wave velocity never exceeds the 'calculation wave velocity'; that is the time-step is small enough that information over this time interval cannot pass physically from one element to the next (Cundall and Board, 1988). FLAC updates coordinate positions using displacements calculated from the previous time-step, which is easily done as there is no global stiffness matrix to invert. The grid therefore is displaced along with the material it represents. To simulate geologic processes, models may be run either to static equilibrium or to failure. The way the dynamic equations of motion are included in the formulation assures that with non-linear materials the numerical scheme utilized is stable even when the physical process being modeled may not be. For our applications, the simulation is 'pseudo-static'. Kinetic energy is both generated and dissipated during the simulation and is manifest as transient inertial 'spikes' within the model.

Another advantage of FLAC for this modeling is the relative ease with which interfaces can be built into the model to simulate faults, bedding planes and joints. Interfaces are assigned normal stiffnesses and shear stiffnesses, and coefficient of sliding friction, and can be assigned optional properties such as tensile strength and cohesion. Interfaces can slip and separate or can be 'glued' to prevent slippage and separation.

The behavior of the rock continuum in our studies is described by Mohr–Coulomb plasticity, which involves a yield function and a non-associated plastic flow rule, formulated in terms of effective stress, not total stress, in plane strain. This represents shear failure in soils and rock masses (Vermeer and de Borst, 1984). The specific constitutive model we use is referred to in FLAC as the strain-softening model. For our simulations, though, we are not making use of the hardening/softening capabilities, rather, for the sake of simplicity we define the material as elastic–perfectly plastic.

One of the most useful and interesting aspects of the code is its ability to simulate localization of plastic deformation. In a given elastic–plastic model, strain may be accommodated either by distributed deformation or by initiation of 'shear bands'. This results from bifurcation in the governing equations, which can lead to localization, even without a strain-softening constitutive relation, provided that the dilation angle is lower than the friction angle (Rudnicki and Rice, 1975; Vardoulakis, 1980). When friction angle and dilation angle are unequal, the situation is referred to as non-associated plasticity (Vermeer and de Borst, 1984), and this is most appropriate for upper crustal geologic materials, in which plastic behavior is combined with pressure-dependent frictional, dilatant behavior (Cundall, 1990). FLAC uses a non-associated plasticity formulation in that the angles of internal friction and dilation are taken as separate parameters. Localization is grid dependent; i.e. if there are enough elements, localization is sure to occur even when using a 'simple' Mohr–Coulomb material. Also, the length scale of localization (thickness of shear bands) is provided by the element size rather than by a physical quantity such as grain size. Shear-band localization occurs partly due to the inclusion of the dynamic equations of motion in the code formulation; shear-band formation releases strain energy which is dissipated within the model in a physically realistic way.

In the models we treat the bands of localized deformation as simulating zones of brittle failure, that is faults. The presence or initiation of a shear-band does not however introduce any additional discontinuity into the numerical model. All interfaces within the models are true discontinuities, and these are created prior to the simulation; all continuous regions remain continuous throughout the simulation.

Model set-up

Geometry. Taking outcrop-scale structures as our prototype (Figs 1 & 2), we set up the basic configuration

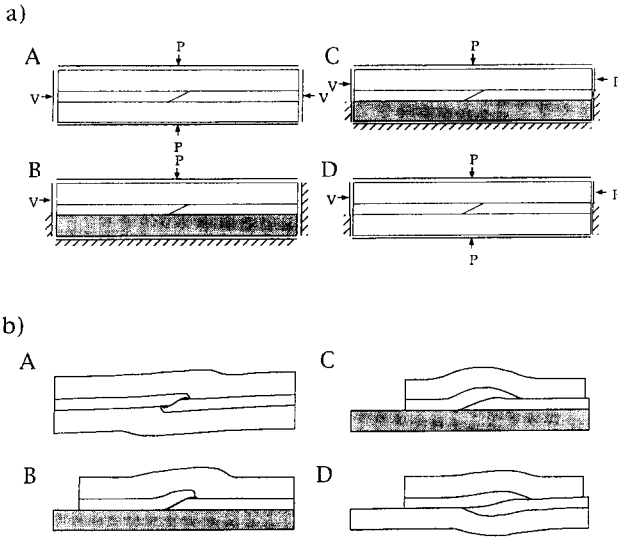

Fig. 3. (a) Boundary conditions for the four numerical models, all with initial dimensions of 20 m × 5 m. V = velocity (displacement/time-step); P = pressure. Hachured pattern indicates the boundary is fixed in the horizontal and vertical directions. Stippled pattern indicates blocks with elastic only behavior. (b) Final geometries of the four models. Maximum displacements are: A, 1.2 m (6% shortening); B, 2.1 m (10.5% shortening); C and D, 4.5 m (22.5% shortening).

of all our models (Fig. 3a). It consists of a simple three-layer sandwich: (1) a 2-m thick 'soft' elastic–plastic upper unit (bread), (2) a 1-m thick elastic–plastic faulted stiff layer (cheese), above (3) a 2-m thick base (bread). The package is 20 m long, and the bottom layer is either an elastic–plastic soft layer capable of large strains (models A and D), or an elastic layer that remains nearly rigid relative to the elastic–plastic units (models B and C). In the latter case this represents a thick, competent unit above which detachment and deformation take place.

The stiff layer contains a simple pre-determined straight interface (fault) that dips 30° toward the left in the center of the model. We have seen such fractures in the field that clearly have become the locus of thrust and fold initiation (Fig. 2a). Conceptually, the stiff layer represents a meter-thick competent limestone unit in between less-competent shale- or clay-rich carbonate layers or, in the case of models B and C, the lower unit represents a nearly rigid structural beam.

Materials. The proper choice of material properties for accurate modeling of geologic phenomena at varying scales is important, yet good data for a number of the parameters are elusive. Data such as the elastic stiffnesses, friction angles, dilation angles, cohesion, etc. of rocks and of joints collected from laboratory-scale specimens may not be appropriate for larger-scale rock systems — even at outcrop scale — due to the ideal intact nature of laboratory specimens as well as the inherent inhomogeneity, anisotropy and discontinuity of field materials. In principle, as the rock mass to be modeled becomes larger, it becomes weaker than a laboratory specimen of the same rock due to an increase in discontinuities or flaws per volume of the larger sample compared to the smaller one. In the extreme, values for the elastic moduli of rocks of as little as 1% of published laboratory values may be appropriate for modeling large-scale rock-mass problems (C. Fairhurst, personal communication). Because of this potential two-order-of-magnitude variation in elastic moduli between laboratory and large-scale samples, one is tempted to simulate phenomena at a smaller rather than a larger scale, because the available data are more likely to be accurate for the simulation. This temptation must be balanced by the need for the models to be accurate at nearly the same scale as the features observed in the field. For this reason we make our models simulate the outcrop scale of several meters. We feel that while published laboratory values of material properties are likely to be somewhat higher than those appropriate for the 'meso-scale' of these models, the variability found in the literature for a given rock type (i.e. limestone or shale) makes accurate material matching difficult. In developing these models, our experience shows that varying the elastic moduli by an order of magnitude or less has an influence on final geometry and structure evolution. Since our intent in making these models is not to match any specific field example, but rather to capture behavior that appears common to many, we have created 'generic' stiff and soft layers using material properties from published analyses of limestone and shale (Goodman, 1980). The material properties used in all simulations are listed Table 1.

Initial and boundary conditions

One of the primary goals of numerical modeling of any phenomenon is to understand how natural examples evolve. For a geologist interested in simulating specific

Table 1. Material properties used in models

	Bulk modulus	Shear modulus	Friction angle	Cohesion	Density
Stiff layer	22.6×10^9 Pa	11.1×10^9 Pa	42°	6.72×10^6 Pa	2.6 kg m^{-2}
Soft layers	8.8×10^9 Pa	4.3×10^9 Pa	14°	38.4×10^6 Pa	2.69 kg m^{-2}
	Normal stiffness	Shear stiffness	Friction angle		
Fault	1×10^{11} Pa m^{-1}	1×10^{11} Pa m^{-1}	5°		
Bedding	1×10^{11} Pa m^{-1}	1×10^{11} Pa m^{-1}	1°		

field examples as well as more general types of fault/fold geometry this requires some physical understanding of the natural system and some trial-and-error in setting up the models. From field observations, one can postulate several different boundary conditions that may be appropriate for fault-related folding, all involving an initial state of a fault ramp cutting across a competent layer. Structural observations on the proximity, orientation and sense of movement on any nearby faults or, say, the presence of a layer-parallel shortening (LPS) fabric (Geiser, 1988) help determine appropriate stress or displacement boundary conditions to apply to the edges of the model domain. In our simulations the boundary conditions in each model do not change during each model run. Geologic evidence, however, might indicate an evolution in boundary conditions with time. This could be investigated. One of our simulations involves overall horizontal shortening in 'pure shear' (Fig. 3a, A), because the field evidence favors this for structural initiation at the earliest stages of shortening within an evolving fold–thrust belt (Fig. 2a; Geiser and Engelder, 1983). Three involve 'far-field' differential displacement of the hangingwall over the footwall at the proximal end of the block (Fig. 3a, B–D), and one of these involves no differential displacement at the distal end (Fig. 3a, B). Because we are beginning with four models that have identical initial geometries and material properties (except that in models B and C the basal units have elastic-only constitutive laws), the differences in evolution of the models are due to differences in the imposed boundary conditions.

All models are brought to equilibrium in an elastic state using a confining pressure of -1.324×10^8 Pa on all four sides of the model, which is equivalent to an overburden of 5 km given an overburden density of 2700 kg m^{-2} (we are using the convention that negative pressures are compressive). Since these are 'pseudo-static' simulations, equilibrium is considered to be achieved when the maximum unbalanced force within the model drops to an appropriately low value relative to the applied load and remains low. For these simulations this occurs with unbalanced forces of about 1×10^6 Pa. Once static equilibrium is achieved, boundary conditions are applied to the model and time-stepping begins. There are three principal types of boundary conditions used in the models: velocity (displacement), stress, and fixed (where the boundary is fixed in x and y in space). There is also what we refer to as the P' condition (Fig. 3a), which is required by the evolving geometry of models C and D and will be described below.

Model A: paired fault-propagation style folds without through-going fault (A, Fig. 3a & b). Model A is the simplest. The boundary conditions are essentially equivalent to a uniaxial compression test with the axis of compression oriented horizontally and a confining pressure, P (lithostatic load), applied to the top and bottom sides of the model. The shortening is achieved by applying a velocity, V, of 0.05 mm per time-step at both ends of the model in opposite directions.

Model B: fault-propagation style fold without through-going fault (B, Fig. 3a & b). In this model the right boundary is fixed. The left side is split, with a rightward velocity of 0.1 mm per time-step applied to both the middle stiff layer and upper soft layer. The upper and lower boundaries have an applied compressive lithostatic load, and the base block is not allowed to deform plastically. The bottom side is fixed.

Model C: fault-bend style fold (C, Fig. 3a & b). Model C has the boundary conditions usually associated with fault-bend style folds. The base is fixed. The left side is as in model B; split with a right-directed velocity of 0.1 mm per time-step applied to the unit above the base. The right side is split with a compressive modified pressure, P', applied to the hangingwall and fixed below the split. The top has an applied lithostatic load. The values of P and P' are the same except that the boundary on which P' acts is modified in the following way. With a split right side the hangingwall will 'fall' off the side of the model as it gets translated against the applied load. This is clearly a geometric artifact of the model that can be dealt with numerically in a number of ways. It could be done by making the footwall block longer, or by supporting the hangingwall block in the 'air' so that it does not exert unwanted moments on the model. We have chosen another tack, which utilizes FLAC's macro language. We monitor the location of the furthest right-hand node of the hangingwall, just above the fault, relative to the furthest right-hand node of the footwall. If this hangingwall node is pushed to the right of the footwall node (i.e. is overhanging), then the column of grid elements to the left of the 'offending' hangingwall node is eliminated. This has the effect of lightening the hangingwall each time a column is eliminated, and this could adversely and unrealistically effect the model by unbalancing the system. However, by monitoring maximum unbalanced forces within the models we are confident that accelerations resulting from this are not significant.

Model D: wedge-folds with through-going fault (D, Fig. 3a & b). Model D is a hybrid of models A and C: The top and bottom are subjected to lithostatic loads, and the lower block is deformable. The left side is split between the base and stiff layer, with a velocity of 0.1 mm per time-step applied to the upper layers, while the right side is split between the upper block and stiff layer. Lateral movement of the upper block is resisted by an applied compressive stress, P', equivalent to the lithostatic load.

RESULTS

In each model run, data defining the current state were saved after every 3000 time-steps (0.3 m displacement). This allows us to 're-occupy' the model at various stages and investigate its evolution. We ran the models until they could progress no further under the given boundary conditions, or until we were satisfied with the amount of displacement (Fig. 3b). The maximum total displacement of the left end of the hangingwall was 4.5 m in models C and D.

In all models the applied loads caused both slip on the interfaces and internal deformation of hangingwall and footwall, mostly associated with the fault ramp. At the earliest stage of the experiments slip occurs first either at the fault ramp (model A) or at the left boundary (models B, C, D), and in all models plastic deformation occurs first in the ramp region. Both slip and plastic deformation occur in an uneven manner that reflects the build-up and dissipation of energy. Principal stresses are generally horizontal and vertical, except in the vicinity of the ramp, where maximum compression is at a high angle to the ramp at zones of contact and local variations are often marked. Zones of incremental shear-strain, as revealed by the 'snapshot' every 3000 time-steps, occur sporadically and in transient pulses throughout the model run.

It is most instructive to follow the evolution of the magnitudes of finite shear-strain (displacement based), γ_{max}, and incremental shear-strain (velocity based), $\dot{\gamma}_{max}$, and track the relationship between the two (see Figs 4 & 5). As would be expected, contoured plots of finite shear-strain, viewed at successive stages of a simulation, show a gradual increase in amount and in area of rock 'damage'. Zones of incremental shear-strain however, viewed at the same time-step, may or may not coincide with zones of high finite strain, although obviously their integration over time yields the finite strain. They are typically organized into bands and occur as transient pulses. The evolution of incremental strain shows that there is a stochastic element to the pattern of development of these fault–fold systems. A zone of failure develops and then is deactivated as stresses are relieved and build-up elsewhere. Many zones are then later reactivated. Since there is no strain softening or weakening in our models, activation and reactivation are favored not by changes in material properties, but by the local variability of the stress state associated with unloading and redistribution of stresses following failure events.

Also present in these models are void spaces that open along interfaces in response to movement of hangingwall over footwall, causing a mismatch in shape once displacement has occurred. Voids are most clearly evident in models A and B in the cores of the asymmetric folds, and they are also present in the early stages of models C and D, but are later reduced to very thin gaps along the fault surface. The voids, which are areas of low pressure, may simply be part of the early evolution of these structures, and in natural examples may be preserved in the field as calcite or quartz in-fillings.

The initial orientation of the fault ramp is 30°, and it appears that with increased displacement there is a tendency for the ramp angle to be reduced in all models. In this respect there is a progression from model A, which has the least amount of displacement and almost no change in ramp angle, through model B with somewhat more displacement, to models C and D which have significantly larger displacements.

Model A

With loading conditions similar to those of a displacement-controlled uniaxial compression test, there can be no through-going fault in model A (Fig. 3b, A). Slip occurs on the fault ramp, but decays quickly in both directions along the flats towards the ends of the model, where no slip is possible. The result is an antisymmetric structure with overturned folds of opposite vergence above and below. With progressive shortening, voids open up along the fault adjacent to the wedge-tips of the stiff layer. Severe distortion of the wedge tips and opening of voids caused problems with the mesh, and the model 'locked up' after only 1.2 m of displacement (6% shortening).

Finite shear-strain is concentrated in the soft layers in well-defined zones that extend from and are nearly parallel to the pre-existing ramp in the stiff layer. The shear-zones act to transfer displacement from the fault surface into the surrounding soft layers. Because of the small total displacement there is little plastic strain recorded in the stiff layers; what strain there is, is concentrated in the overturned wedge-tip. There is no significant reduction of the ramp angle.

Model B

This configuration, with restraint on the lower layer and push at the left end applied only to the stiff layer and upper soft layer, restricts folding to the hangingwall and produces a structure that is similar to a fault-propagation or fault-tip fold (Suppe, 1985; Jamison, 1987) (Fig. 3b, B). Slip is transferred from the lower flat, up the ramp to the upper flat, where it dies out in an asymmetric fold. The fold fore-limb is nearly vertical and the vergence is in the hangingwall transport direction. In this case, no plastic deformation of the lower soft layer was allowed; it was kept elastic *a priori*. As in model A, a void appears at the top of the ramp.

As in model A, distortion of the wedge tip and the void opening caused mesh problems that limited maximum displacement, in this case to 2.1 m (or 10.5% shortening). Conjugate zones of high finite shear-strain are located in both the upper soft layer and the stiff layer where it is bent to accommodate movement over the ramp. The two zones intersect at the footwall ramp. The more intense one, associated with forward thrusting, is parallel to and extends upwards from the ramp in the stiff layer (best

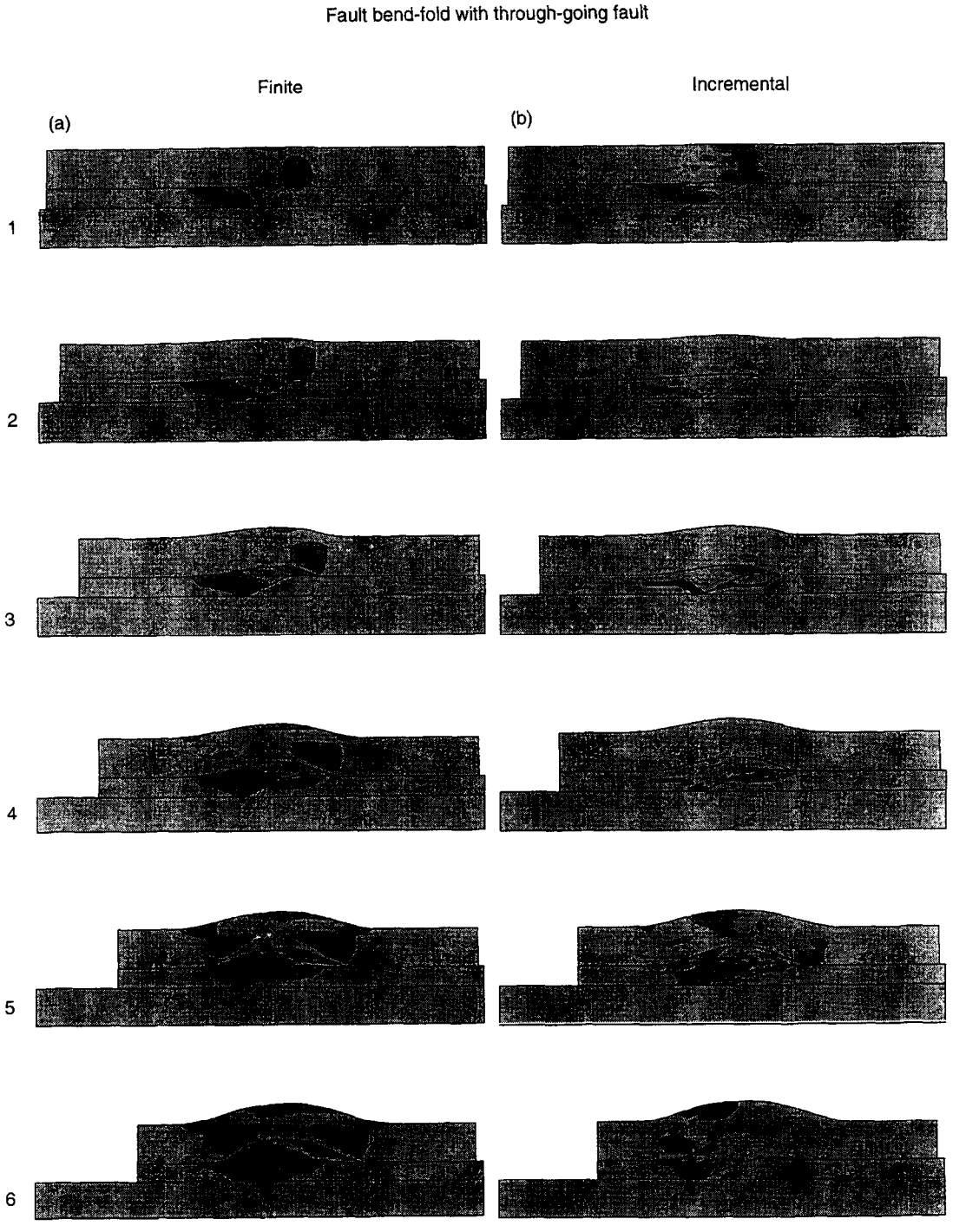

Fig. 4. Sequential diagrams illustrating the evolution of model C, at 0.3, 0.9, 1.8, 2.7, 3.6 and 4.5 m displacement respectively. (a) Contours of maximum finite shear-strain, γ_{max}; the value at stage 6 is 0.6. (b) Contours of maximum incremental shear strain (strain rate), $\dot{\gamma}_{max}$; the value at stage 6 is $8.0 \times 10^{-5}\,sec^{-1}$.

seen in Fig. 6a). The other one dips at a similar angle in the opposite direction, consistent with incipient back thrusting.

Displacement vectors show that displacement is transferred from the fault to the rearward-dipping zone of high shear-strain at the top of the ramp (Fig. 7a).

Model C

This is similar to model B in that the lower soft layer is constrained to lie on a rigid base and is only allowed to deform elastically, but does not restrain the movement of the hangingwall soft layer to the right. These conditions

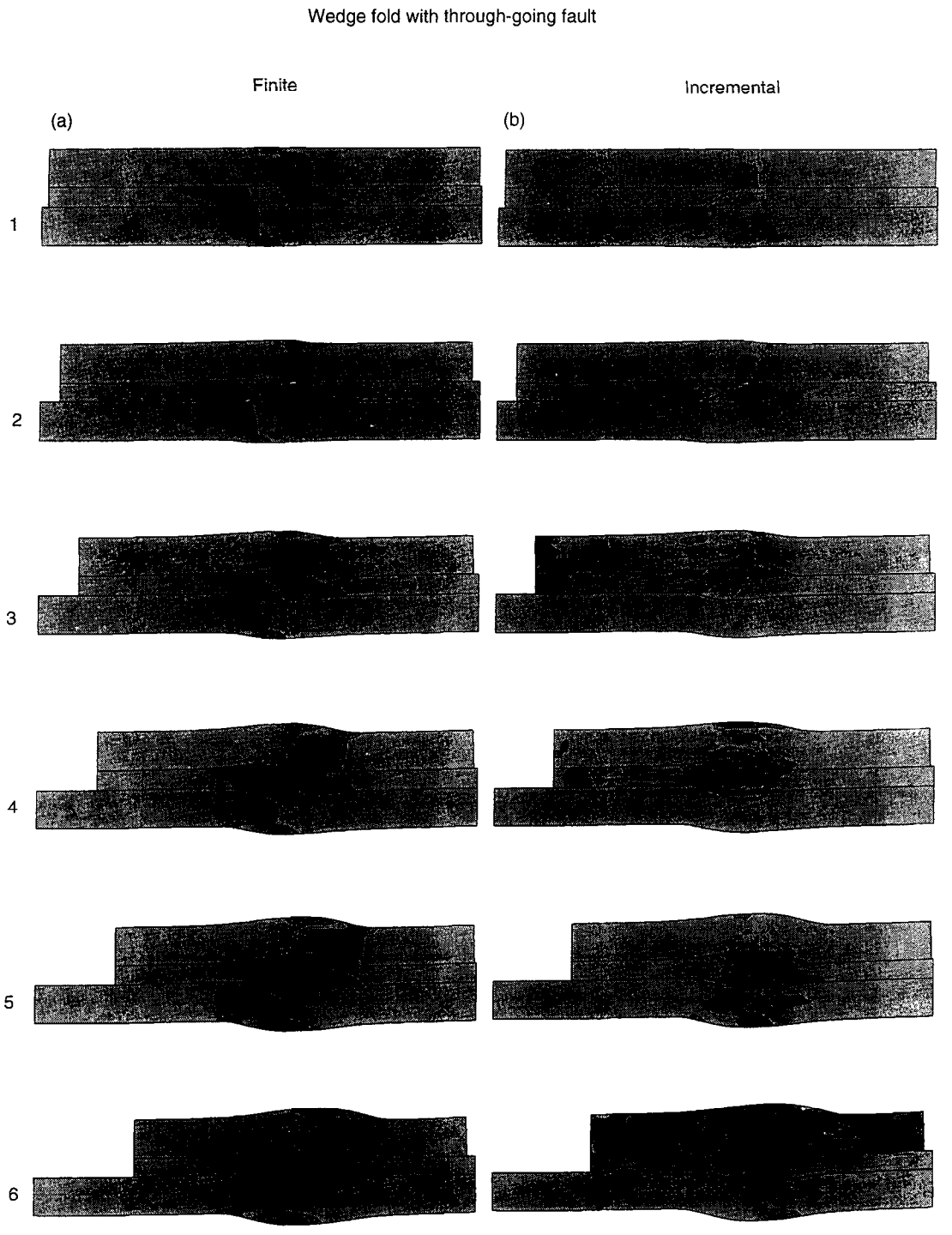

Fig. 5. Sequential diagrams illustrating the evolution of model D, at 0.3, 0.9, 1.8, 2.7, 3.6 and 4.5 m displacement respectively. (a) Contours of maximum finite shear-strain; the value at stage 6 is 0.45. (b) Contours of maximum incremental shear strain (strain rate); the value at stage 6 is 2.5×10^{-5} sec^{-1}.

result in a throughgoing fault and a fault-bend style fold (a ramp anticline) in the hangingwall as it moves over the ramp in the footwall. The interface between the stiff layer and upper soft layer and the upper soft layer itself together form a smooth, basically symmetric fold with gentle limb dips (Fig. 3b, C). A significant footwall bulge (or a low-amplitude anticline) develops in the top of the stiff layer near the top of the footwall ramp (Fig. 4, stages 4–6 and Fig. 10). There are no significant voids along the fault in the final state, but voids are present during the early stages of the model run, and are later reduced to thin gaps along the fault surface.

Finite and incremental shear-strain patterns in the hangingwall (Fig. 4) show that a forward-dipping zone of high incremental and finite shear-strain develops in the hangingwall as it moves from flat to ramp. This zone stays fixed with respect to the footwall while a widening zone of finite shear-strain develops in the hangingwall.

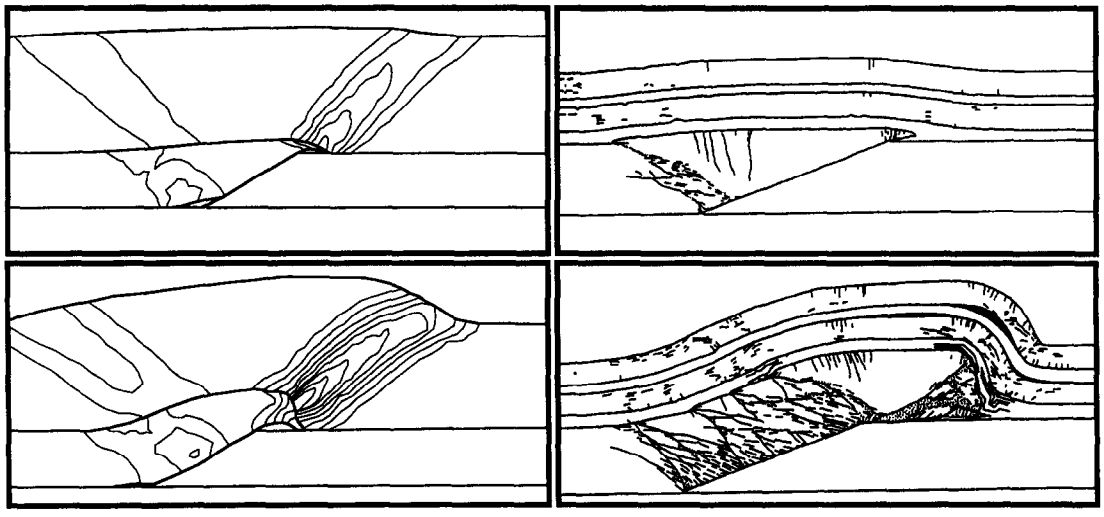

Fig. 6. Comparison between our model B at two stages (a) and the experimental models of Chester *et al.* (1991) (Fig. 5) using rocks (b). (a) Contours of finite shear strain in model B indicate areas of brittle–plastic deformation. Contour interval is 0.05 in upper and 0.1 in lower figure, with maximum finite shear strains of 0.25 and 0.9. (b) Line drawings of rock models of Chester *et al.* (1991) show areas of strong brittle–plastic deformation which match the strain distribution seen in (b).

Displacement patterns for model C (Fig. 7b) differ strongly from those of model B (Fig. 7a), and clearly show the effect of a throughgoing fault.

Model D

This differs from model A only in two end boundary conditions, which cause a throughgoing fault to become activated with net rightward displacement of the hangingwall. The result is an antisymmetric wedge-fold with open, nearly symmetric folds in the soft layer above and below the ramp. There is significant flattening of the ramp angle with increasing displacement. As in model C, there are no significant voids along the fault in the final state, but voids are present during the early stages of the model run, closing up as the ramp becomes

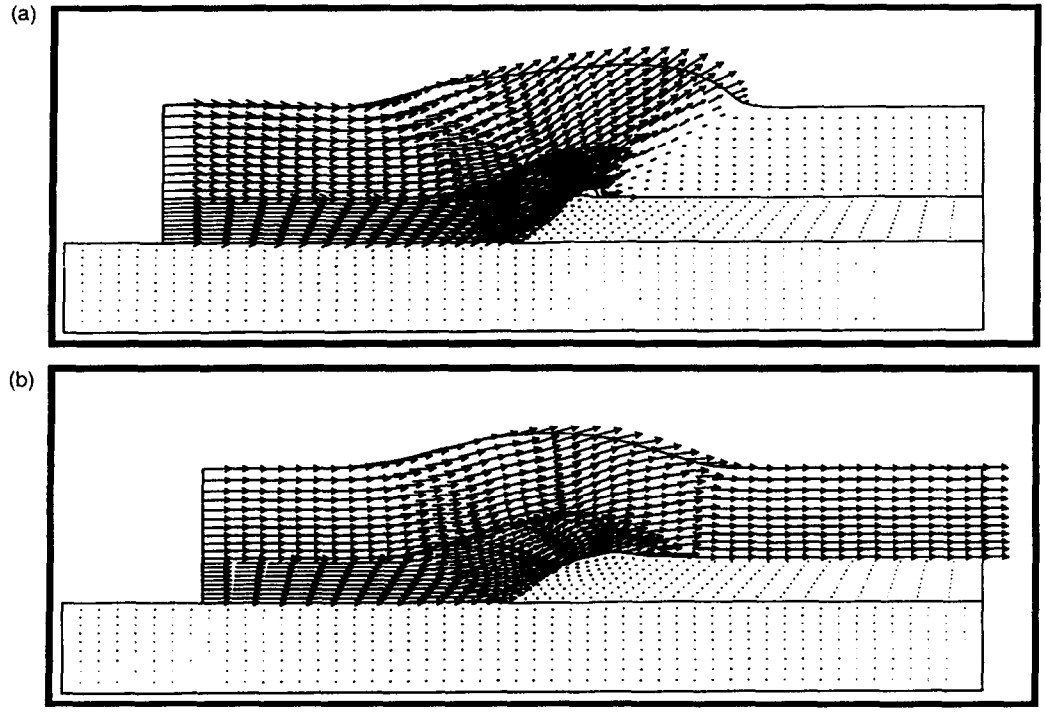

Fig. 7. Plots of displacement vectors at intermediate stages of shortening in two models. (a) Model B. Displacement is transferred from the fault surface at the ramp up into the soft layer as a result of the non-slip end condition imposed on the right side, yielding a displacement field associated with fault-propagation style folds. (b) Model C. Releasing the upper right-side boundary, allowing slip, produces a smooth displacement field over the ramp, consistent with fault-bend style folds.

more gentle and the angularity of the ramp flat transition reduced.

Patterns of finite shear-strain are essentially identical in the hangingwall and footwall (Fig. 5). By the end of the run, they show two diffuse conjugate zones of shear, one forward-dipping and the other backward-dipping, which cross in the center of the model. The deformation is less intense in the soft layers, and more intense within the stiff layer. Within the stiff layer, most evident at an early stage of deformation, zones of high strain lead away from the bends in the fault surface, each zone making a conjugate pair with the 'zone' represented by slip on the fault ramp (Fig. 5a, stages 1, 2). These zones become wider as the simulation progresses (Fig. 5a, stages 3–6). Comparison of patterns of incremental shear-strain and finite shear-strain (Fig. 5) at various times in the simulation shows that zones of incremental shear-strain stay fixed with respect to the bends in the fault while the zones of high finite shear-strain move with the hangingwall and footwall up and down the ramp, respectively. As it migrates past the bends in the fault, the hangingwall accumulates 'damage', creating widening zones of finite shear-strain. The same is true for the footwall.

This model and model C are not restricted by fixed right-side boundaries like models A and B, and therefore they can be run to an arbitrary displacement. Both models were taken to a 4.5 m maximum displacement (22.5% shortening).

FAILURE MAPPING

The areas affected by incremental and finite plastic deformation can be represented graphically by maps as in Figs 4 and 5, and these show the likely location of faults or areas of general cataclastic deformation in the material. Further insight into the evolution of rock failure within an evolving structure can be gained by plotting magnitudes of stresses at a given location as a function of 'time'. We can imagine possible stress paths for sedimentary rocks that may become involved in thrust belt tectonics. Initially a rock mass might be close to a lithostatic state of stress ($\sigma_1 = \sigma_2 = \sigma_3$) as it experiences burial. This can result only in volumetric strain. Later, due to regional compression it may deviate from this state and deform elastically, but not reach the yield stress. At some point the differential stress may become great enough to cause the material to yield, and plastic flow begins. The material may remain at yield and continue to deform plastically, or it can return to an elastic state, perhaps to return to yield one or more times. Such stress histories are represented in our models and we investigate them using σ_1–σ_3 plots (Fig. 8).

An advantage of treating failure in principal stress space rather than Mohr (τ–σ) space is that it is graphically much simpler (Jaeger and Cook, 1969, p. 88). The stress state is represented by a point rather than by a circle. A bigger advantage is that by plotting any stress state as a point, the evolution of stress state with time is represented as a line.

The Mohr–Coulomb failure criterion can be written in terms of principal stresses (Paterson, 1978) as:

$$\sigma_1 = \sigma_3 N_\phi - 2C_o\sqrt{N_\phi}, \tag{1}$$

where:

$$N_\phi = \frac{1 + \sin\phi}{1 - \sin\phi}, \tag{2}$$

and where σ_1 and σ_3 are the maximum and minimum principal stresses, respectively; C_o is the material cohesion and ϕ is the angle of internal friction.

This failure condition is shown by a solid straight line in Fig. 8. On the σ_1–σ_3 plots in Fig. 8, stress states above the failure envelope (solid line) are stable (i.e. elastic), stress states at plastic yield lie on the envelope. The starting states for our models are represented by the stars in Fig. 8. They are close to a lithostatic state of stress, which is represented by the dashed line.

Failure plots

We present in Fig. 8 stress plots for model C only. Eight points were chosen in the middle of the hangingwall half of the stiff layer. They are labeled according to the numbering scheme for nodes within the model, and are selected in order to illustrate the behavior in the region that moves over the footwall ramp. Note that the vertical and horizontal scales on the stress plots are unequal. Although there are significant differences, these plots have some features in common. (1) The initial stress state at all locations within the fold is basically the same, being nearly lithostatic. It represents the pressure applied to simulate an overburden of 5 km. For failure to occur, there must be either an increase in σ_1, a decrease in σ_3 or a combination of the two. (2) There is a general movement to the right after the simulation begins, corresponding to an increase in σ_1, which results from stresses induced by the horizontal shortening of the model prior to displacement on the fault. (3) Yield is reached in all 8 locations for varying amounts of time.

The jerky nature of the paths reflects stress changes accompanying the discrete slip events on the fault and the initiation of shear bands. As expected, there is a direct correlation between the form of the stress plot (Fig. 8) and the finite and incremental strain history (Fig. 4). The relative amount of time that the stress path stays on the failure envelope corresponds to the total amount of 'damage' or finite strain that accrues in a particular location within the model. For instance, locations 10, 12, 14 and 16 all spend a significant amount of time on the failure envelope and are in locations within the model that show high finite shear-strain. These contrast with locations 20 and 22, which spend most of the model runtime in elastic space, and are at locations within the model that show very little finite shear-strain. When the

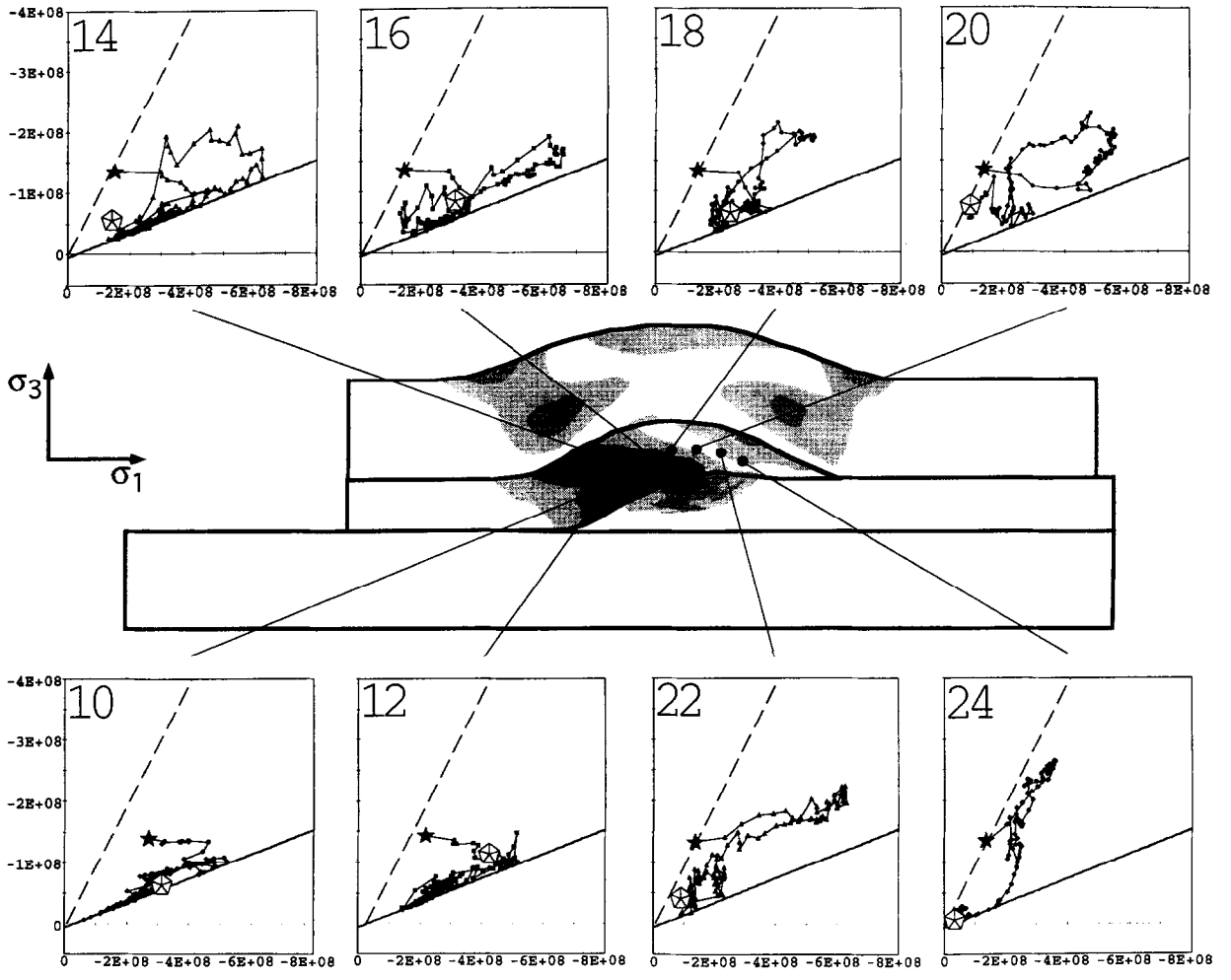

Fig. 8. Plots to track failure at selected locations within the hangingwall ramp anticline in model C. Contours in the central panel are of finite shear strain, identical to those of Fig. 4(a) (stage 6). The plots show the evolution of the stress state in principal stress space. The vertical axis is σ_3 and the horizontal is σ_1. Note the scales are not similar. The initial state is marked by a black star and the final state by a white star/pentagon. The failure envelope is the solid line and lithostatic stress state ($\sigma_1 = \sigma_3$), the dashed line. Location numbers are element nodes in the model. The amount of finite strain or 'damage' that occurs at a given location in the model is a function of the amount of run-time spent on the failure envelope.

stress path is on the failure envelope, the location concerned lies within a zone of high shear-strain-rate.

DISCUSSION

Fractures at the proper angle for becoming thrust ramps are common in competent beds in some fold-and-thrust belts (Fig. 2a), and there is little doubt that at least some of these become activated as ramps and lead to the development of the kind of fault-related folds displayed by our models. How these fractures originate in the first place is beyond the scope of this paper. There is little evidence, however, given the planarity of the strata in some locations, that they were caused by an increase of stresses on the limbs of earlier-formed buckle folds (Dixon and Liu, 1992; Liu and Dixon, 1995), but rather, may have formed in the earliest stages of fold-and-thrust belt evolution as shear fractures related to horizontal shortening (Gretener, 1972; Eisenstadt and De Paor, 1987). All of the basic fold–fault relationships produced in the models (Fig. 3) have their counterparts in rocks and in physical model experiments. Wedge folds, with footwall and hangingwall roughly equally affected (Fig. 3b, D), are common in nature (Fig. 1a, Cloos, 1961, 1964; Martinez-Torres *et al.*, 1994), at least at the outcrop scale. Natural fault-propagation style folds (Fig. 3b, B) are also common and have been produced in non-scaled experiments using rocks (Fig. 6b, Chester *et al.*, 1988, 1991). Fault-bend style folds (Fig. 3b, C) are the most classical of fault-related folds (Rich, 1934; Suppe, 1985) and many natural examples exist (e.g. Fig. 1b). In both experiments of Chester *et al.* and in our models, the factor that determines whether a fault-propagation style fold or fault-bend style fold develops is the 'resistance to foreland translation' relative to 'resistance to internal deformation'. It seems likely that this relative resistance could be affected either by the local mechanical conditions (i.e. strength of the layers involved), or by differences in far-field loading caused by development of

structures on a larger scale. That is, once a ramp has developed elsewhere, the forces favoring foreland translation will be increased. What determines whether or not the footwall becomes deformed depends largely on the rigidity of the strata below the affected stiff layer. The one style of structure in the models that seems uncommon in nature is the paired fault-propagation style fold (Fig. 3b, A). Martinez-Torres *et al.* (1994, fig. 2c) have illustrated a structure that is of this type.

There is a striking similarity between the pattern of deformation in the hangingwall stiff layer as it moves up and over the ramp in our models, in the physical models of Chester *et al.* (1988, 1991) (Fig. 6b), and in the analog models of Morse (1977). In all three a progressive sequence of back-thrusts develops in the hangingwall from the flat–ramp transition in the footwall, and the strained or 'damaged' rock thus formed is then carried somewhat passively up the ramp. A second, but less intense, zone of fractured rock develops in the tip of the hangingwall wedge as it moves over the upper ramp-flat transition. These phenomena are expressions of fold hinge migration. In our models, most of the folds are broad with poorly defined hinges. The pattern of asymmetry of deformation in the ramp anticline in model C (Figs 3b, C & 4a), with the back-limb more highly strained than the fore-limb, might not be taken in a natural fold as resulting from hinge migration. The lack of angularity of all our folds, except those at the tip of the wedges in fault-propagation type folds, is striking.

Perhaps the most significant feature of our models, not present in other numerical models of fault-related folding, is the localization of deformation, induced by stress bifurcation. This simulates faulting in the brittle regime (Vermeer and de Borst, 1984; Cundall, 1990). Localization occurs as a consequence of the adoption of a non-associated plasticity constitutive relationship in the model. This mechanism of localization differs from those, such as strain softening or fabric softening, normally associated with deformation in ductile materials. Rudnicki and Rice (1975) and Vardoulakis (1980) showed that even if the material does not soften, given a dilation angle lower than the friction angle (non-associated plasticity), localization will occur even in the hardening regime: so called 'stress-state softening' (Cundall, 1990). This is what is occurring in our models, in which the dilation angle is 0°. Localization occurs numerically due to extremely small effects such as slight perturbations of the grid from one time-step to another due to inertial forces. The effect is illustrated in Fig. 9. When localization occurs, the stress in one zone is decreased compared to the stress in the immediately adjacent material. Despite the reduction in stress, material in the affected zone — a shear band — is at failure, whereas that outside is not (Fig. 9a & b). The normal and shear stress across the shear band interface must be the same, and this results in stress refraction across the boundary and principal stresses within the band at nearly 45° to the boundary

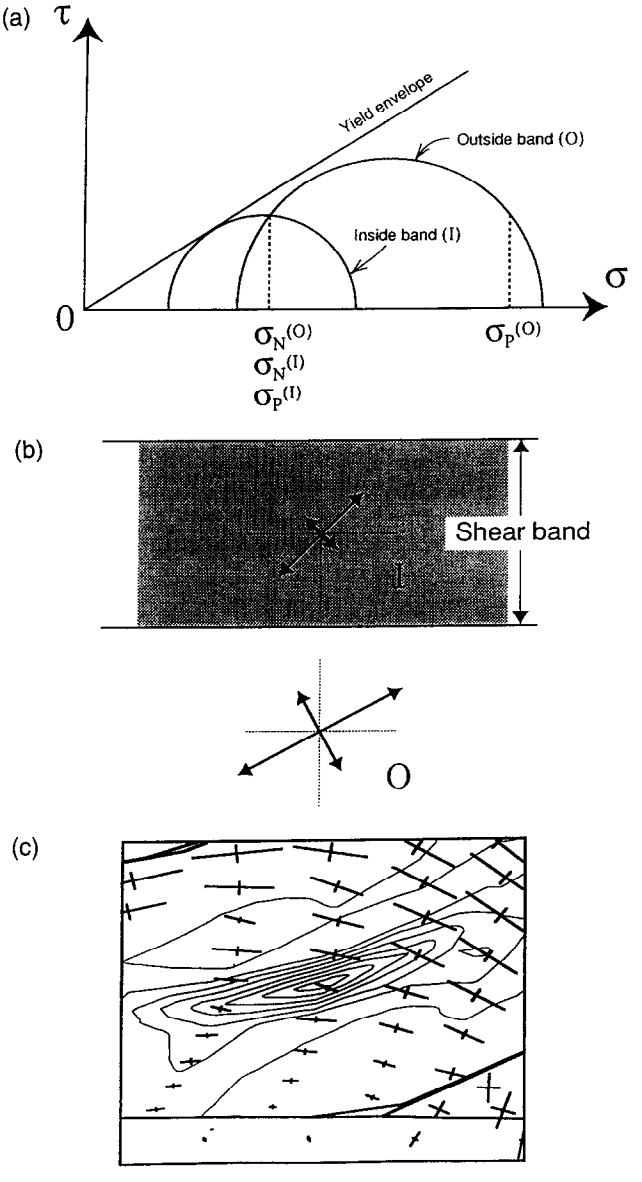

Fig. 9. (a, b) Schematic illustration of stress state bifurcation and localization associated with the formation of shear bands in a cohesionless material (after Cundall, 1990). (a) Mohr diagram showing stresses inside (*I*) and outside (*O*) the shear band immediately after localization. Stresses parallel to the band indicated by subscript *P* and stresses normal to the band by subscript *N*. (c) Detail from model C at stage 5 (see Fig. 4), showing the relationship between incremental shear strain (strain rate), defining a shear band as indicated by the contours, and principal stress orientation. Stresses within the shear band are smaller than outside and are oriented at approximately 45° to the shear band boundary.

(see Cundall, 1990). An example from model C (stage 5) is shown in detail in Fig. 9(c).

Besides the prominent shear bands or faults that develop in back-thrust orientation in the hangingwall in our models, there are other patterns of interest. One of these is the appearance of zones of failure in the footwall (Fig. 10) that represent the incipient shearing off of the top of the ramp and collapse of the footwall. This represents either the initiation of duplex development or a horse that may become carried with the hangingwall.

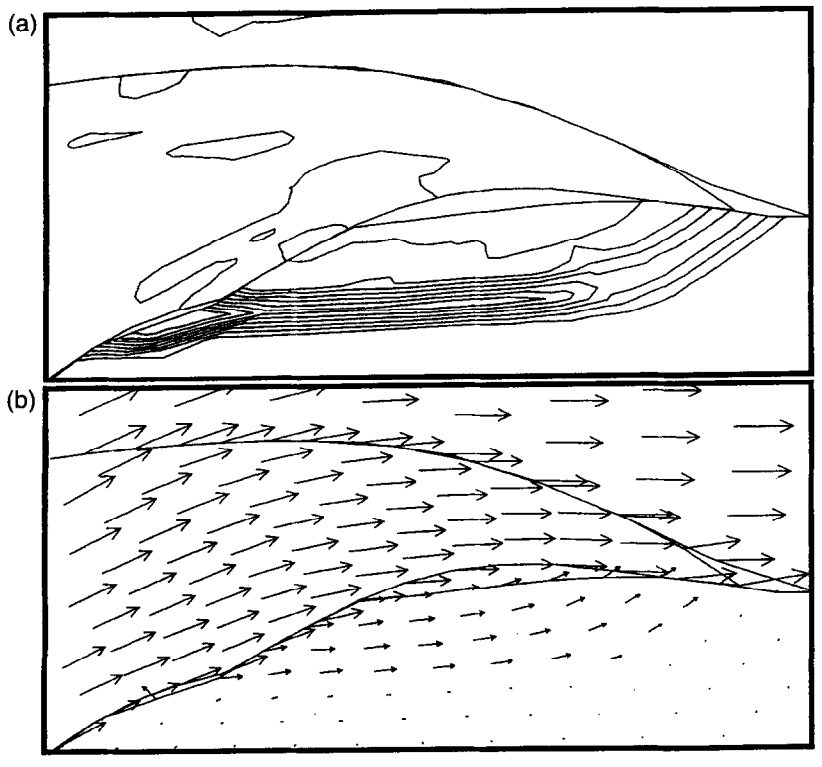

Fig. 10. Detail at an intermediate stage (between stages 4 and 5 of Fig. 4b) of a fault-bend style fold near the top of the fault ramp. (a) Contours of shear strain rate in the footwall show a ramp–flat geometry associated with duplex formation. (b) Velocity vectors show differential movement in the footwall ramp region indicating incipient footwall collapse and duplex formation.

This incipient footwall collapse is manifest as zones of high finite shear-strain that have the familiar ramp–flat geometry within the continuous stiff layers (Fig. 10a). Such behavior is present in models B, C and D, the last having them in both the hangingwall and footwall, and it is related to and likely the cause of the slight bulges that are present in the footwall stiff layers of models B and C, and in the early stages of model D.

An interesting pattern is shown in Figs 9(c) and 4(a) in which bedding-parallel failure occurs in the stiff layer to form shear bands in the synclinal hinge of the hangingwall. This is very similar to the phenomenon noted by Kuenen and De Sitter (1938) in folding experiments with thick clay slabs. It represents initiation of flexural slip in otherwise massive layers. Occasionally several parallel such shear bands occur, the spacing of which depends on the mesh size. The phenomenon of spaced shear bands is not inherent to mesh geometry, as shown by Cundall (1990).

Another feature of the models is that deformation associated with shear bands does not proceed in an orderly and predictable manner, but rather occurs in fits and starts that represents turning on and off of individual faults or shear bands. This phenomenon is associated with the build-up and release of elastic energy in the models. To a greater or lesser extent it is present in all the models.

The rather symmetric fold shapes in our models C and D (Figs 4 & 5) are similar to the shapes of folds produced in other models of ramp-related folding in which there is low resistance to slip on the fault, including the viscous flow analytical models of Berger and Johnson (1980) and Kilsdonk and Fletcher (1989), and the finite-element models involving plastic deformation and viscous flow of Erickson and Jamison (1995). The mechanism by which the hangingwall accommodates movement over the ramp, however, is quite different in these various models. Deformation in the viscous flow models is broadly distributed, and such flow could simulate either crystal–plastic processes (which behave as non-linear fluids) or diffusive mass transfer in rocks, depending on conditions under which thrusting occurs. Deformation in the models of Erickson and Jamison (1995) is less broadly distributed, with plastic failure occurring in the hangingwall above fold hinges, and viscous strain developing in similar locations, but also in the footwall where pressure is high yet differential stresses are less and therefore insufficient to cause failure. Pressure-dependent plasticity in the models of Erickson and Jamison (1995) and in our models simulates deformation involving fracture and frictional slip in upper crustal rocks. However, the non-associated plasticity in our models, not present in the models of Erickson and Jamison, leads to the development of localization in ours. Each localization event, examples of which are captured in the incremental strain plots of Figs 4 and 5, simulates a new fracture zone developing and some associated increment of plastic strain. The strain associated with these events accumu-

lates to build up zones of 'damage', especially evident in the hangingwall as it moves up the ramp (Figs 4a & 5a). Unlike rocks, however, the material in our model is not weakened by the accumulation of strain, because no strain softening or hardening is incorporated into the flow rule.

Our models simulate best near-surface crustal conditions in which the dominant deformation mechanism is fracture and frictional slip. These conditions also are appropriate to the physical models of Chester *et al.* (1991) and analog models of Serra (1977). The deformation pattern is very similar in all of these. It is likely, in nature, that varying slip rates and ramp angles, which will affect the stress level that builds up, will cause different mechanistic response in rocks under the same general physical conditions. Knipe (1985) showed how the deformation mechanisms in the hangingwall will depend on the geometry of the ramp and rate of slip. Slow slip rates and gentle ramps favor diffusive mass transfer, intermediate conditions favor crystal–plastic flow, while fast slip rates and high ramp angles favor brittle behavior and possible truncation of the top or base of the ramp (Knipe, 1985). Ramp truncation is well developed in our model C, in which the footwall shows incipient collapse. The slower-rate mechanisms described by Knipe are not simulated by our models.

In all our models there is a tendency for the ramp angle to decrease with increasing displacement on the fault. This is most pronounced when both hangingwall and footwall are deformable (Fig. 3b, D). By reducing the ramp angle, the resistance to deformation and the distortion of the hangingwall and footwall are reduced. This phenomenon was noted in the physical model experiments by Morse (1977) and in the natural examples described by Serra (1977). It is the opposite of what would occur if homogeneous shortening developed in the layer without slip on the fault, as would occur under conditions of slow slip and diffusive mass transfer (Knipe, 1985).

CONCLUSIONS

A variety of fold styles were developed in our numerical models of deformation at thrust ramps involving elastic behavior and failure, fault slip, and pressure-sensitive plastic flow. Under conditions that restrict throughgoing faulting, antisymmetric fault-propagation style folds develop in both hangingwall and footwall. With rigid footwall and restricted distal slip in the hangingwall, a single fault-propagation style fold develops. With distal displacement of the hangingwall allowed, the ramp forms a perturbation on an otherwise flat and unbounded fault, and broader antisymmetric wedge folds develop if hangingwall and footwall are both deformable. A single fault-bend style fold develops if the footwall is rigid. All structures become accentuated as slip increases on the fault. If both hangingwall and footwall are deformable, the deformation reduces the ramp angle and tends to minimize distortion of the rock adjacent to the fault.

The structures produced in our models all have counterparts in nature, and we believe that the cause of the variation in style of folds associated with fault ramps may be the same in nature and in experiment. In the models, behavior is controlled by varying the boundary conditions, and this is likely to be the case in nature also, where loading of the boundaries of the zone in which the structure is to develop depends on 'far-field' structure, stratigraphy, and stresses. Effects similar to those due to varying the boundary conditions could be obtained by varying material properties of the rock layers and the pre-existing faults and bedding planes. Whether by varying boundary conditions (as we demonstrate here) or by varying material properties, there appear to be two important factors that determine the style of structures developed: (1) the relative resistance to foreland translation versus internal deformation (Chester *et al.*, 1991), and (2) the extent to which the footwall is deformable. A systematic parametric study would help elucidate this further. It is important to note that our models do not simulate the non-brittle deformation mechanisms of diffusive mass transfer or crystal–plastic flow, which are active in ramp-associated deformation under suitable conditions, and which help determine the geometry of the structures developed (Knipe, 1985).

While we examined here only the early stages of development of fault-related folds, we believe that many structures on all scales in fold-and-thrust belts have evolved from the kind of structures we have modeled. With evolution of natural 'far-field' boundary conditions from general early-stage sub-horizontal shortening (Geiser and Engelder, 1983) to overall simple shearing associated with large thrust systems, some of these structures will become the locus for significant regional slip, while others will become preserved as incipient structures as in Fig. 2.

It is likely that, as deformation proceeds, it becomes progressively more difficult to trace the origins of particular structures as being of fault-bend or fault-propagation type, as noted by Liu and Dixon (1995) in their physical models. Also, although many folds in fold-and-thrust belts are likely to originate from deformation associated with displacement at thrust ramps, others probably develop by buckling and subsequently become associated with thrusting (Fischer *et al.*, 1992; Liu and Dixon, 1995). Numerical modeling may help us understand better the evolution of these different types of structure, and provide criteria for distinguishing among them. This could be done by comparing the spatial and temporal evolution of failure and deformation in model and nature, using plots of incremental or finite shear-strain in the models (Figs 4 & 5) and making maps of fracture intensity and inference of principal stress orientations in natural structures (Wickham *et al.*, 1982). In addition, techniques such as failure mapping

(Fig. 8) allow us to evaluate the discrete nature of deformational activity associated with fault-related folding, and give us a better idea of how the structures we observe in their final state may develop.

Acknowledgements—We thank Peter Cundall, Mark Board and the staff of Itasca Consulting Inc. for sharing with us their invaluable insight, and Christian Teyssier and the U of M structural geology group for lively discussions. We also thank John Dixon, an anonymous reviewer, and Don Fisher for their insightful reviews and comments. This work was partially supported by a Grant-in-Aid to P. J. H from the Graduate School of the University of Minnesota, and by Research Grants to L. M. S. from the Geological Society of America and the American Association of Petroleum Geologists.

REFERENCES

Apperson, K. D. and Goff, D. F. (1991) Deformation of thrust ramps and footwalls observed in numerical models. *EOS* **72**, 514–515.

Berger, P. and Johnson, A. M. (1980) First-order analysis of deformation of a thrust sheet moving over ramp. *Tectonophysics* **70**, T9–T24.

Boyer, S. E. (1986) Styles of folding within thrust sheets: examples from the Appalachian and Rocky Mountains of the U.S.A. and Canada. *Journal of Structural Geology* **8**, 325–339.

Boyer, S. E. and Elliott, D. (1982) Thrust systems. *Bulletin of the American Association of Petroleum Geologists* **66**, 1196–1230.

Chapple, W. M. (1978) Mechanics of thin-skinned fold-and-thrust belts. *Bulletin of the Geological Society of America* **89**, 1189–1198.

Chester, J. S., Spang, J. H. and Logan, J. M. (1988) Comparison of thrust fault rock models to basement-cored folds in the Rocky Mountain foreland. *Memoirs of the Geological Society of America* **171**, 65–74.

Chester, J. S., Logan, J. M. and Spang, J. H. (1991) Influence of layering and boundary conditions on fault-bend and fault-propagation folding. *Bulletin of the Geological Society of America* **103**, 1059–1072.

Cloos, E. (1961) Bedding slips, wedges, and folding in layered sequences. *Bulletin de la Commission Géologique de Finlande* **33**, 106–122.

Cloos, E. (1964) Wedging, bedding plane slips, and gravity tectonics in the Appalachians. *Memoirs of the Department of Geological Sciences, Virginia Polytechnic Institute* **1**, 63–70.

Coetzee, M. J, Hart, R. D., Varona P. M. and Cundall, P. A. (1995) *FLAC Basics*. Minneapolis, Itasca Consulting Group.

Cundall, P. A. and Board, M. (1988) A microcomputer program for modeling large-strain plasticity problems. In *Numerical Methods in Geomechanics, Proceeding of the 6th International Conference on Numerical Methods in Geomechanics*, ed. C. Swoboda, pp. 2101–2108. A. A. Balkema, Rotterdam.

Cundall, P. A. (1990) Numerical modelling of jointed and faulted rock. In *Mechanics of Jointed and Faulted Rock*, ed. J. Rossmanith, pp. 11–18. A. A. Balkema, Rotterdam.

Dahlen, F. A. and Barr, T. D. (1989) Brittle frictional mountain building 1. Deformation and mechanical energy budget. *Journal of Geophysical Research* **94**, 3906–3922.

Dahlen, F. A., Suppe, J. and Davis, D. (1984) Mechanics of fold-and-thrust belts and accretionary wedges: cohesive Coulomb theory. *Journal of Geophysical Research* **89**, 10,087–10,101.

Dahlstrom, C. D. A. (1969) Balanced cross-sections. *Canadian Journal of Earth Sciences* **6**, 743–757.

Dahlstrom, C. D. (1970) Structural geology in the eastern margin of the Canadian Rocky Mountains. In *29th Annual Field Conference, Wyoming Geological Association Guide*, pp. 407–439.

Davis, D., Suppe, J. and Dahlen, F. A. (1983) Mechanics of fold-and-thrust belts and accretionary wedges. *Journal of Geophysical Research* **88**, 1153–1172.

Dixon, J. M. and Liu, S. (1992) Centrifuge modelling of the propagation of thrust faults. In *Thrust Tectonics* ed. K. R. McClay, pp. 53–69. Chapman and Hall, London.

Eisenstadt, G. and De Paor, D. G. (1987) Alternative model of thrust-fault propagation. *Geology* **15**, 630–633.

Elliott, D. (1976) The motion of thrust sheets. *Journal of Geophysical Research* **81**, 949–963.

Elliott, D. and Johnson, M. R. W. (1980) Structural evolution of the northern part of the Moine thrust belt, NW Scotland. *Transactions of the Royal Society of Edinburgh, Earth Science* **71**, 69–96.

Erickson, S. G. (1995) Mechanics of triangle zones and passive-roof duplexes: implications of finite-element models. *Tectonophysics* **245**, 1–11.

Erickson, S. G. and Jamison, W. R. (1995) Viscous–plastic finite-element models of fault-bend folds. *Journal of Structural Geology* **17**, 561–573.

Fischer, M. P., Woodward, N. B. and Mitchell, M. M. (1992) The kinematics of break-thrust folds. *Journal of Structural Geology* **14**, 451–460.

Geiser, P. A. (1988) Mechanisms of thrust propagation: some examples and implications for the analysis of overthrust terranes. *Journal of Structural Geology* **10**, 1149–1156.

Geiser, P. and Engelder, T. (1983) The distribution of layer-parallel shortening fabrics in the Appalachian foreland of New York and Pennsylvania: Evidence for two non-coaxial phases of the Alleghenian orogeny. *Memoir of the Geological Society of America* **158**, 161–175.

Goodman, R. E. (1980) *Introduction to Rock Mechanics*. John Wiley and Sons, New York.

Gretener, P. E. (1972) Thoughts on overthrust faulting in a layered sequence. *Bulletin of Canadian Petroleum Geology* **20**, 583–607.

Jaeger, J. C. and Cook, N. G. W. (1969) *Fundamentals of Rock Mechanics*. Methuen and Co. Ltd, London.

Jamison, W. R. (1987) Geometric analysis of fold development in overthrust terranes. *Journal of Structural Geology* **9**, 207–209.

Kilsdonk, B. and Fletcher, R. C. (1989) An analytical model of hangingwall and footwall deformation at ramps on normal and thrust faults. *Tectonophysics* **163**, 153–168.

Knipe, R. J. (1985) Footwall geometry and the rheology of thrust sheets. *Journal of Structural Geology* **7**, 1–10.

Kuenen, P. H. and De Sitter, L. U. (1938) Experimental investigation into the mechanisms of folding. *Leidsche Geologische Medeelingen* **10**, 217–240.

Lan, L. and Hudleston, P. J. (1995) Angular folds developed in single layers and rheological implications. *Geological Society of America Abstracts with Programs* **27**, 123.

Liu, S. and Dixon, J. M. (1995) Localization of duplex thrust-ramps by buckling: analog and numerical modelling. *Journal of Structural Geology* **17**, 875–886.

Martinez-Torres, L. M., Ramon-Lluch, R. and Eguiluz, L. (1994) Tectonic wedges: geometry and tectonic interpretation. *Journal of Structural Geology* **16**, 1491–1494.

McClay, K. R. (1992) *Thrust Tectonics*. Chapman and Hall, London.

Mitra, S. and Namson, J. (1989) Equal-area balancing. *American Journal of Science* **199**, 563–599.

Morse, J. (1977) Deformation in ramp regions of overthrust faults: experiments with small-scale rock models. In *29th Annual Field Conference, Wyoming Geological Association Guide*, pp. 457–470.

Paterson, M. S. (1978) *Experimental Rock Deformation — The Brittle Field*. Springer-Verlag, Berlin.

Ramsay, J. G. (1967) *Folding and Fracturing of Rocks*. McGraw-Hill, New York.

Ramsay, J. G. (1992) Geometrical problems with ramp-flat models. In *Thrust Tectonics*, ed. K. R. McClay, pp. 191–200. Chapman and Hall, London.

Reddy, J. N. (1993) *An Introduction to the Finite Element Method*. McGraw-Hill, New York.

Reddy, J. N., Stein, R. J. and Wickham, J. S. (1982) Finite-element modeling of folding and faulting. *International Journal of Numerical and Analytical Methods in Geomechanics* **6**, 425–440.

Rich, J. L. (1934) Mechanics of low-angle overthrust faulting as illustrated the Cumberland thrust block, Virginia, Kentucky, and Tennessee. *Bulletin of the American Association of Petroleum Geologists* **76**, 1584–1596.

Rudnicki, J. W. and Rice, J. R. (1975) Conditions for the localization of deformation in pressure-sensitive dilatant materials. *Journal of the Mechanics and Physics of Solids* **23**, 371–394.

Serra, S. (1977) Styles of deformation in the ramp regions of overthrust faults. In *29th Annual Field Conference, Wyoming Geological Association Guide*, pp. 487–498.

Suppe, J. (1983) Geometry and kinematics of fault-bend folding. *American Journal of Science* **283**, 684–721.

Suppe, J. (1985) *Principles of Structural Geology*. Prentice Hall, Englewood Cliffs, N.J.

Suppe, J. and Medwedeff, D. A. (1984) Fault-propagation folding. *Geological Society of America Abstracts with Programs* **16**, 670.

Vardoulakis, I. (1980) Shear band inclination and shear modulus of sand in biaxial tests. *International Journal of Numerical and Analytical Methods in Geomechanics* **4**, 103–119.

Vermeer, P. A. and de Borst, R. (1984) Non-associated plasticity for soils, concrete and rock. *Heron* **29**, 1–64.

Wickham, J. S., Tapp, G. S. and Reddy, J. N. (1982) Finite-element modelling of fracture density in single layer folds. *International Journal of Numerical and Analytical Methods in Geomechanics* **6**, 441–459.

Woodward, N. B. (1992) Deformation styles and geometric evolution of some Idaho–Wyoming thrust belt structures. In *Structural Geology of Fold and Thrust Belts*, ed. S. Mitra and G. W. Fisher, pp. 191–206. Johns Hopkins University Press, Baltimore.